



Temperature and state-of-charge estimation in ultracapacitors based on extended Kalman filter

Chia-Jui Chiang*, Jing-Long Yang, Wen-Chin Cheng

Department of Mechanical Engineering at National Taiwan University of Science and Technology, Taipei 10607, Taiwan, ROC

HIGHLIGHTS

- Simultaneous estimation of ultracapacitor SOC and temperature is achieved via EKF algorithm.
- The extended model includes voltage-and-thermal-dependent equivalent circuit and thermal dynamics.
- Satisfactory prediction over applicable frequencies is achieved via weighted least squares.
- The impact of modeling errors becomes more significant at temperature below freezing point.
- The EKF-based estimator is robust to modeling errors and measurement noises even at low temperature.

ARTICLE INFO

Article history:

Received 26 September 2012

Received in revised form

23 January 2013

Accepted 25 January 2013

Available online 9 February 2013

Keywords:

Ultracapacitor

Extended Kalman filter

State of charge

Thermal dynamics

Nonlinear equivalent circuit model

Modeling error

ABSTRACT

The performance and life expectancy of ultracapacitors depend heavily on the operating voltage and temperature. In this paper, simultaneous estimation of state-of-charge (SOC) and temperature is achieved by applying extended Kalman filter (EKF) algorithm with only the terminal measurement of voltage and current. For the application of EKF algorithm, a nonlinear model which consists of a voltage-and-thermal-dependent equivalent circuit model and a thermal model is first developed. The parameters in the equivalent circuit model are identified by applying least squares method with weightings at different frequencies so as to achieve satisfactory prediction over the whole applicable frequency ranges. Experimental results demonstrate that the EKF-based estimator is crucial in providing accurate and consistent prediction of SOC and temperature in existence of modeling errors and measurement noises, especially during dynamic charge/discharge cycles at low temperature. The accurate estimation of SOC and temperature enables optimum energy and thermal management of ultracapacitors.

© 2013 Elsevier B.V. All rights reserved.

1. Introduction

Ultracapacitors (UCs), also known as supercapacitors or electrochemical double-layer capacitors (EDLCs), are electrical energy storage devices which offer higher specific power density, higher efficiency and longer shelf and cycle-life than batteries [1–3]. These advantages have enabled potential applications of ultracapacitors such as consumer electronics, electric/hybrid vehicles, and industrial power management [4–8]. The performance and life expectancy of ultracapacitors, however, depend heavily on not only the operating voltage but also the cell temperature [1,9].

The voltage and thermal dependence and thermal dynamics of ultracapacitors have been studied in a couple of works [1,2,9–13].

Temperature dependence of the capacitance and equivalent series resistance (ESR) is investigated in Ref. [10] for ultracapacitors with different electrolytes. Based on the data obtained at various temperatures and voltages, accelerated aging factors for an increase of maximal cell voltage and for an increase of temperature are determined. In Ref. [11], temperature effect on self-discharging rate is studied and ultracapacitor modules with cooling elements and forced cooling are designed. More recently in Ref. [12], the temperature effect on electrolyte resistance and ESR is further analyzed and the results indicate that an increase in temperature decreases the electrolyte viscosity and increases the electrolyte ionic self-diffusion coefficient and thus raises the degree of dissociation and ionic mobility. A heat generation model, which consists of irreversible Joule heat and reversible heat caused by change of entropy, is proposed in Ref. [1]. A holistic simulation model is developed in Ref. [9] by combining the heat generation model in Ref. [1] with an electrical model and an aging model to study the

* Corresponding author.

E-mail address: cjchiang@mail.ntust.edu.tw (C.-J. Chiang).

long-term behavior of the ultracapacitors. Concurrently with Ref. [9], a three-dimensional heat conduction model is used in Ref. [2] to study the temperature distribution of the capacitor cell during charge and discharge cycles. More recently in Ref. [13], thermal-electric models are applied for thermal modeling and heat management of ultracapacitor modules in vehicle applications and the simulation results indicate that a forced airflow cooling system is necessary.

Voltage and thermal dependent equivalent circuit models have been developed to describe the electrical behavior of ultracapacitors [14–17]. In Ref. [14], a dynamic model is developed in frequency domain using electrochemical impedance spectroscopy (EIS) and transformed into time domain for simulation. Three parameters, including a series resistance, a capacitance and a time constant, are considered dependent on temperature and voltage and need to be identified from the impedance measurements at various operating conditions. In Ref. [15], the double-layer capacitance is modeled by two parallel resistive capacitive branches with different time constant. The capacitance is linearly and cubically dependent on voltage and temperature respectively, whereas the resistance is a cubic function of temperature. In Ref. [16], an equivalent circuit model is developed with 14 RLC components linearly dependent on voltage and/or temperature. More recently in Ref. [17], the equivalent circuit model in Ref. [14] is adopted and parameters in the model are identified using artificial neural networks (ANNs) with temperature and voltage measurement.

In most applications [4–8], ultracapacitors are used either for boost in peak power or for regeneration of electrical energy. Therefore, for optimum energy and thermal management, accurate estimation of the state of charge (SOC) and temperature of the ultracapacitors is necessary. Conventionally, SOC is estimated via the open-circuit voltage (OCV) of the capacitor in an equivalent RC series circuit neglecting the thermal dependence [7,8]. The thermal effect on the electrical characteristics, however, is significant [12,15] and needs to be considered in estimating SOC. The experimental results in Fig. 1 demonstrate the impact of temperature. Charged with the same current profile, the terminal voltage V_T raises faster at -35°C due to the declined capacitance. In this paper, simultaneous estimation of SOC and temperature is achieved by applying the stochastic extended Kalman filter (EKF) technique to an extended model containing a voltage-and-thermal-dependent equivalent circuit model and a thermal model. EKF has been widely used to estimate SOC and state-of-health (SOH) of batteries for its ability to take modeling uncertainties and measurement noises into consideration in simultaneous estimation of multiple states and parameters [18–21]. Several variants of Kalman filter such as central difference Kalman filter (CDKF) [22,23] and unscented Kalman filter (UKF) [24,25] have also been applied to battery SOC estimation providing even better estimates at the expense of higher complexity and computational cost [26]. Few studies about application of the Kalman filter techniques to the estimation of ultracapacitor states, however, have been reported.

The extended model used in this paper contains an equivalent circuit model which is developed based on the approach in Ref. [14] by conducting EIS tests at different operating voltages and temperatures. Since in the EIS tests less data points are generated at lower frequencies, the least squares method may result in less accuracy at the lower frequency ranges as illustrated in Ref. [14] and Fig. 4. In this paper, to minimize the prediction error at the whole frequency range the ultracapacitor is charged and discharged, weightings at different frequency ranges are applied to the least squares method. Moreover, a thermal model which include the heat generation model in Ref. [1] and a simple heat transfer model is augmented in the extended model for temperature estimation. The Experimental implementation results show that assuming the

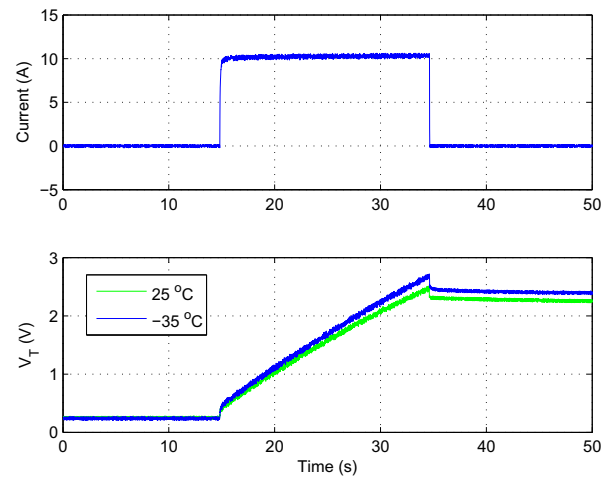


Fig. 1. Thermal effect on the electrical behavior of a 100 F PowerBurst ultracapacitor.

heat transfer conditions are given the EKF-based estimator achieves improved and consistent estimation of SOC and temperature with only the terminal measurement of voltage and current at different operating conditions. The benefit of applying the EKF algorithm becomes more significant during dynamic charge/discharge cycles at extremely low temperature as the impact of modeling uncertainties becomes more noteworthy.

2. Experimental setup

Fig. 2 shows the experimental setup used in this study. All the tests are conducted on Tecate's PowerBurst ultracapacitors, with a nominal capacitance of 100 F, a rated voltage of 2.7 V, and an operating temperature range from -40°C to 65°C . The PowerBurst ultracapacitor adopts the cylindrical construction method. The cells are constructed from activated carbon particles, mixed with a blinder and then deposited on aluminum foil. The non-water soluble electrolyte increases the withstand voltage per cell and thus produces higher energy density than the water-soluble electrolyte. Different sets of ultracapacitor are used in the impedance measurements and in the charge/discharge cycle tests so modeling errors are expected. The modeling procedure and estimation algorithm used in this paper can be applied to different types of electrical energy storage devices such as batteries and ultracapacitors with higher capacitance.

All the tests are performed in a controlled climatic chamber GCT-120-40SP-AR, which is capable of controlling the temperature within $\pm 0.3^\circ\text{C}$ in the range from -70°C to 100°C . For the model development in Section 3, a Zahner IM6 Electrochemical Impedance Spectrometer is used to measure the cell impedance for temperatures between -40°C and 60°C and voltages between 0.5 V and 2.5 V. The ultracapacitor is polarized with the DC voltages and a 10 mV voltage ripple, with frequency sweeping between 50 mHz and 100 Hz, is superimposed on the DC components. The measurement of the current amplitude and phase with respect to the injected voltage determines the impedance. The charge/discharge cycle tests in Section 5 are carried out by connecting a programmable power supply DSP-008-090HD from IDRC and a programmable electronic load 3310F from Prodigit in parallel, enabling currents of up to 60A. The data acquisition and the EKF estimator are implemented in a PC with NI PCI-6229 board via the MATLAB xPC-target environment. Temperature of the ultracapacitor is measured with a platinum thin-film temperature sensor POK1232.6W.13.008 attached to its surface, which is capable of

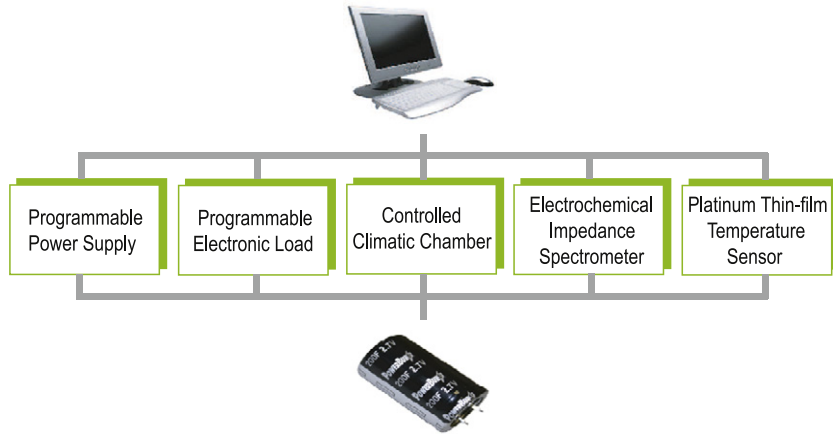


Fig. 2. Experimental setup.

measuring temperature from $-200\text{ }^{\circ}\text{C}$ to $600\text{ }^{\circ}\text{C}$ with $\pm 0.3\text{ }^{\circ}\text{C}$ maximum deviation. The noisy measurement is smoothed out using a moving average to obtain the longer-term trends of the cell temperature. The current is measured using a hall-effect current transducer HY 5-P from LEM, which enables a measuring range of $\pm 15\text{ A}$ with $\pm 150\text{ mA}$ accuracy. The terminal voltage is measured directly with the PC-based NI PCI-6229. By setting the analog input range to $\pm 5\text{ V}$, a voltage measurement accuracy of $\pm 75\text{ }\mu\text{V}$ is achieved.

3. Extended model

EKF estimation requires an extended model which consists of state and measurement equations.

$$\begin{aligned}\dot{x}(t) &= f(x(t), u(t)) + w(t) \\ z(t) &= h(x(t), u(t)) + v(t)\end{aligned}\quad (1)$$

where f and h are nonlinear functions of the extended states and input, $x(t)$ is an extended state vector consisting of the estimated states, $u(t)$ is the input vector, $z(t)$ is the measured output, $w(t)$ is the process noise, and $v(t)$ is the measurement noise. Section 3.1 describes the extended model which consists of a voltage and thermal dependent equivalent circuit model in Section 3.1.1 and a thermal model in Section 3.1.2. The parameters in the model are then identified in Section 3.2.

3.1. Model description

3.1.1. Equivalent circuit model

The equivalent circuit model is developed based on the approach in Ref. [14]. The impedance of the ultracapacitor is expressed as:

$$Z(j\omega) = R_s + \frac{\tau \cdot \coth(\sqrt{j\omega\tau})}{C \cdot \sqrt{j\omega\tau}} \quad (2)$$

where R_s is the equivalent series resistance (ESR), C is the capacitance, τ is a time constant and ω is the operating frequency. The parameters R_s , C and τ are all functions of temperature and voltage which will be identified in Section 3.2.1. The impedance model in Eq. (2) is then transformed into the time domain and can be represented as a serial RC circuit in series with infinite number of parallel RC circuits [14]. For the real-time EKF implementation, the equivalent circuit model is simplified as a serial RC circuit in series with two parallel RC circuits, as shown in Fig. 3, i.e.

$$Z(j\omega) \approx R_s + Z_c(j\omega) + Z_1(j\omega) + Z_2(j\omega) \quad (3)$$

where $Z_c(j\omega)$, $Z_1(j\omega)$ and $Z_2(j\omega)$ are the impedances of the capacitor C , the 1st and 2nd parallel RC circuits in Fig. 3 respectively. The parameters R_1 , R_2 , C_1 and C_2 in the equivalent circuit in Fig. 3 are mathematically determined from the two experimentally determined parameters C and τ [14].

$$C_1 = C_2 = \frac{C}{2} \quad (4)$$

$$R_1 = \frac{2\tau}{\pi^2 C}, \quad R_2 = \frac{\tau}{2\pi^2 C}. \quad (5)$$

Therefore, only three parameters R_s , C and τ in the equivalent circuit model in Fig. 3 need to be determined based on the impedance measurements at different operating conditions in Section 3.2.1.

3.1.2. Thermal model

Temperature dynamics of the ultracapacitor is described by a thermal model including the heat generation model in Ref. [1] and a simple heat transfer model.

$$\frac{dT(t)}{dt} = \frac{1}{C_{\text{heat}}} \left[\frac{dQ_{\text{joule}}(t)}{dt} + \frac{dQ_{\text{rev}}(t)}{dt} - Ah(T(t) - T_0) \right] \quad (6)$$

where $T(t)$ is temperature of the ultracapacitor, T_0 is the ambient temperature, C_{heat} is heat capacitance of the ultracapacitor, A is the effective heat transfer area (surface area of the ultracapacitor), and h is the heat transfer coefficient. The heat generation in ultracapacitor is the superposition of the irreversible Joule heat dQ_{joule}/dt and the reversible heat dQ_{rev}/dt [1]. The Joule heat dQ_{joule}/dt

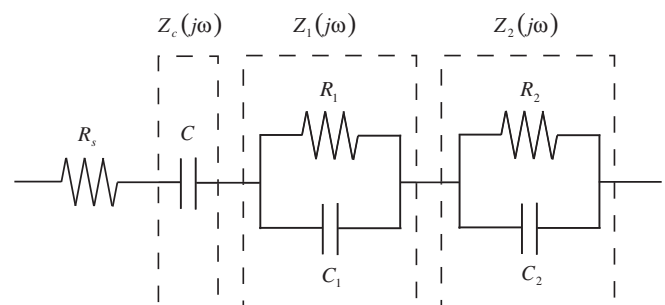


Fig. 3. RC series-parallel equivalent circuit.

results from the power loss in the ohmic resistances which can be derived from the equivalent circuit model in Fig. 3.

$$\frac{dQ_{\text{Joule}}(t)}{dt} = i^2(t)R_s + i_1^2(t)R_1 + i_2^2(t)R_2 \quad (7)$$

where $i(t)$ is the charging current, $i_1(t)$ and $i_2(t)$ are the current through the resistance R_1 and R_2 in Fig. 3 respectively. On the other hand, the reversible heat dQ_{rev}/dt results from entropy changes due to the ion movement in the electrolyte [1,9]

$$\frac{dQ_{\text{rev}}(t)}{dt} = \frac{2k_b a}{e} i(t) T(t) \quad (8)$$

where $k_b = 1.380658 \times 10^{-23} \text{ J K}^{-1}$ is the Boltzmann constant, $e = 1.602 \times 10^{-19} \text{ C}$ is the elementary charge, and a is a factor depending on the geometry of the ultracapacitor [1].

Combining the voltage and temperature dependent equivalent circuit model in Fig. 3 and the thermal model from Eqs. (6) to (8), the extended model which consists of 4 state equations and 1 measurement equation can be summarized based on the general form in Eq. (1):

$$\begin{bmatrix} \dot{\text{SOC}} \\ \dot{V}_1 \\ \dot{V}_2 \\ \dot{T} \end{bmatrix} = \begin{bmatrix} 0 & 0 & 0 & 0 \\ 0 & -\pi^2 \frac{1}{\tau} & 0 & 0 \\ 0 & 0 & -4\pi^2 \frac{1}{\tau} & 0 \\ 0 & \frac{\pi^2 V_1 C}{2C_{\text{heat}} \tau} & \frac{2\pi^2 V_2 C}{C_{\text{heat}} \tau} & -\frac{Ah}{C_{\text{heat}}} \end{bmatrix} \begin{bmatrix} \text{SOC} \\ V_1 \\ V_2 \\ T \end{bmatrix} + \begin{bmatrix} \frac{1}{C(V_{c,\text{max}} - V_{c,\text{min}})} \\ \frac{2}{C} \\ \frac{2}{C} \\ \frac{2k_b a T}{e C_{\text{heat}}} + \frac{R_s i}{C_{\text{heat}}} \end{bmatrix} i + \begin{bmatrix} 0 \\ 0 \\ 0 \\ \frac{AhT_0}{C_{\text{heat}}} \end{bmatrix} + w(t)$$

$$V_T = [V_{c,\text{max}} - V_{c,\text{min}} \quad 1 \quad 1 \quad 0] \begin{bmatrix} \text{SOC} \\ V_1 \\ V_2 \\ T \end{bmatrix} + R_s i + V_{c,\text{min}} + v(t) \quad (9)$$

where the first state SOC is the state-of-charge determined from the open-circuit voltage V_c of the capacitor C in Fig. 3, V_1 and V_2 are voltages of the 1st and 2nd parallel RC circuits in Fig. 3, and the final state T is the temperature of the ultracapacitor. The input is the current i whereas the output is the terminal voltage V_T .

3.2. Parameter identifications

3.2.1. Identification of parameters in the equivalent circuit model

The three parameters R_s , C and τ in the simplified impedance model (3) are identified based on the electrochemical impedance spectrometer (EIS) measurements of the ultracapacitor at different voltages and temperatures, as described in Section 2. To minimize the prediction error in the whole frequency range, the ordinary linear least-squares method is modified with weightings at different frequencies.

$$R_s, C, \tau \frac{1}{2} \sum_{\omega_i = \omega_0}^{\omega_n} a_{\omega_i} \left[(Re_{\omega_i}(R_s, C, \tau) - Re_{\omega_i, \text{data}})^2 + (Im_{\omega_i}(R_s, C, \tau) - Im_{\omega_i, \text{data}})^2 \right] \quad (10)$$

where $Re_{\omega_i}(R_s, C, \tau)$ and $Im_{\omega_i}(R_s, C, \tau)$ are the real part and imaginary part of the simplified impedance model (3) at frequency ω_i

respectively, $Re_{\omega_i, \text{data}}$ and $Im_{\omega_i, \text{data}}$ are the real part and imaginary part of the EIS measurement at frequency ω_i respectively, and a_{ω_i} is the weighting at frequency ω_i . The weighted linear least squares regression is solved with the MATLAB Curve Fitting Toolbox in which either Cholesky decomposition or orthogonal decomposition can be employed. As an example at 1 V and 20 °C, Fig. 4 compares the impedance measurement against the prediction of the models derived with and without weightings at different frequencies. The ordinary linear least-squares method without weightings (dashed line) results in less accuracy at lower frequencies since less data points are generated at lower frequencies in the EIS test. With higher weightings at lower frequencies, the accuracy at lower frequencies is improved at the cost of a slight loss of accuracy at higher frequencies. In practice, depending on the applications, the weightings can be tuned for satisfactory prediction over the applicable frequency ranges.

Similar procedure is repeated at various voltages (0.5 V, 1 V, 1.5 V, 2 V and 2.5 V) and various temperatures (−40 °C to 60 °C) to obtain the voltage and temperature dependence of the parameters R_s , C and τ , as shown in Fig. 5. As voltage increases, the series resistance R_s drops whereas the capacitance C and the time constant τ raise.

The rise of capacitance at higher voltage may result from the increase of electrolyte electric constant, the reduction of the distance separating the charges at the electrode/electrolyte interface, or the increase of charge displacement inside the electrode [16]. The temperature dependence of the parameters R_s , C , τ is more significant at temperature below freezing point due to the

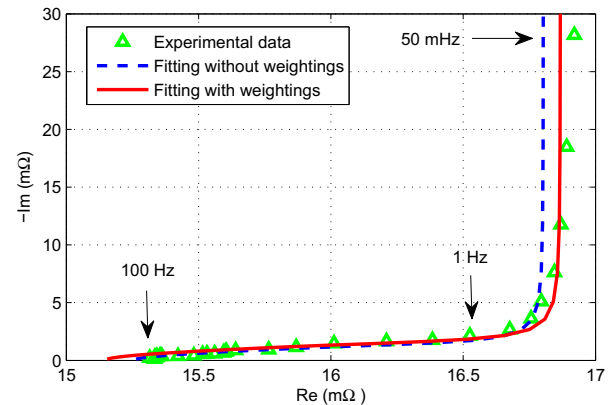


Fig. 4. Comparison of the impedance measurement against the predictions of the models derived with and without weightings at different frequencies at 1 V and 20 °C.

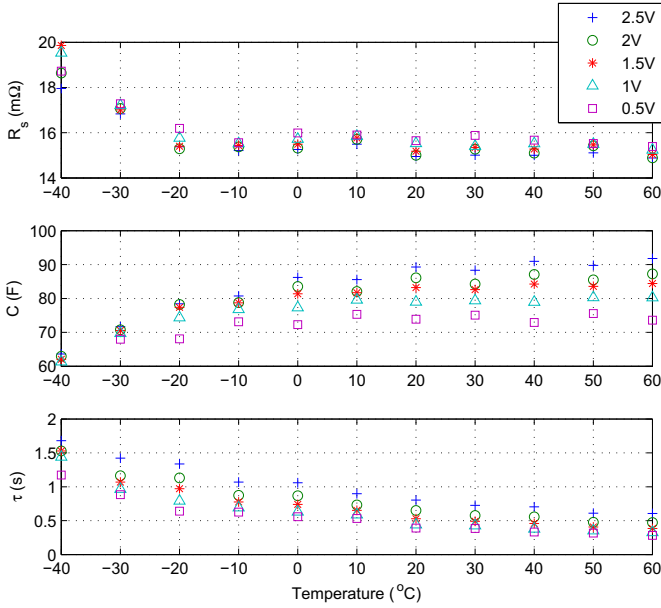


Fig. 5. Voltage and temperature dependence of the parameters in the equivalent circuit model.

increase of the electrolyte's viscosity at low temperatures limiting ionic transport speed which increases the resistance and drops the capacitance [11–13]. At higher temperatures a second effect becomes important, which combined with the viscosity effect induces the non-monotonic relation of the resistance and capacitance to temperature as shown in Fig. 5 and observed in Refs. [10,11,14,15,17,27]. Specifically, at higher temperatures the increased Brownian motion of the ions extends the average distance of the Helmholtz layer to the electrode surface, which may slightly reduce the capacitance and increase the resistance [11].

Since the application of EKF involves discretization and linearization of Eq. (9) about the current state estimate, it is more convenient to obtain the polynomial approximation of the terms in Eq. (9) R_s , $1/\tau$, C/τ and $1/C$ as functions of the terminal voltage V_T and temperature T .

$$\begin{aligned} R_s &= c_1 T^3 V_T + c_2 T^3 + c_3 T^2 V_T + c_4 T^2 + c_5 T V_T + c_6 T + c_7 V_T + c_8 \\ \frac{1}{\tau} &= c_9 T V_T + c_{10} T + c_{11} V_T + c_{12} \\ \frac{C}{\tau} &= c_{13} T V_T + c_{14} T + c_{15} V_T + c_{16} \\ \frac{1}{C} &= c_{17} T^2 V_T + c_{18} T^2 + c_{19} T V_T + c_{20} T + c_{21} V_T + c_{22} \end{aligned} \quad (11)$$

where the coefficients c_1 – c_{22} are determined by applying least squares method to the data (symbols) in Fig. 6 and their values are listed in Table 2. The resulting polynomial curves are also shown in Fig. 6 as solid lines for validation of the curve fitting. The statistics of the percentage errors of the polynomial approximations in (11) at 55 points is summarized in Table 1. The accuracy can be further improved if higher order polynomials are used at the expense of higher complexity and computational cost. The choice of lower order polynomial approximations is considered legitimate in the sense that the uncertainties and simplifications can be compensated by the EKF algorithm introduced in Section 4.

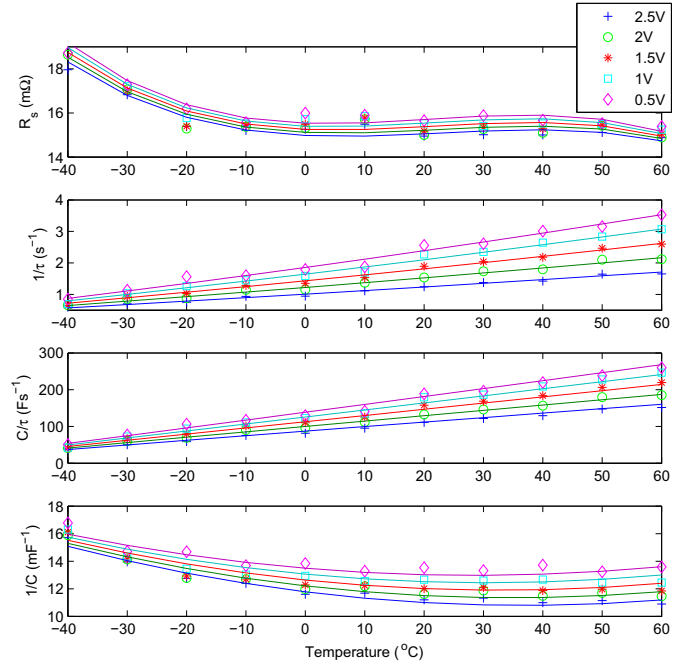


Fig. 6. Polynomial approximation of the voltage and temperature dependent terms in the extended model in Eq. (9).

3.2.2. Identification of parameters in the thermal model

The heat capacitance C_{heat} , the heat transfer coefficient h and the geometric factor a in the thermal model (6) and (8) are identified based on the temperature measurements of the ultracapacitor during charge/discharge cycles under different heat transfer conditions, as shown in Fig. 7. For precise identification of the heat capacitance C_{heat} in Eq. (6), the ultracapacitor along with a platinum thin-film temperature sensor are wrapped with a ceramic fiber blanket for heat insulation ($h = 0$). The heat conductivity of the ceramic fiber blanket is less than $0.08 \text{ W m}^{-2} \text{ K}^{-1}$ at temperature below 400°C . The heat capacitance C_{heat} can thus be identified from the generated heat ΔQ and the temperature rise ΔT obtained from the adiabatic case shown on the left of Fig. 7

$$C_{\text{heat}} = \frac{\Delta Q}{\Delta T} \quad (12)$$

where the generated heat ΔQ is obtained from integration of the Joule heat in Eq. (7). Impact of the reversible heat in Eq. (8) is neglected here due to the short charge/discharge period (10 s). As long as the heat capacitance C_{heat} is known, the heat transfer coefficient h can be identified from the temperature measurement. For instance, with the natural heat dissipation case on the left hand side of Fig. 7, the heat transfer coefficient h is about $13 \text{ W m}^{-2} \text{ K}^{-1}$. On the other hand, the geometric factor a in the reversible heat in Eq. (8) is identified based on temperature measurements of the ultracapacitor during longer charging period. Specifically, for the current profile shown on the right of Fig. 7 under adiabatic condition, the value of factor a is found close to 2.

Table 1
Percentage errors of the polynomial approximations in Eq. (11).

Parameter	R_s % error	$1/\tau$ % error	C/τ % error	$1/C$ % error
Min.	0.048	0.115	0.018	0.005
Max.	5.948	15.708	14.252	6.377
Mean	1.53	3.96	4.22	2.43

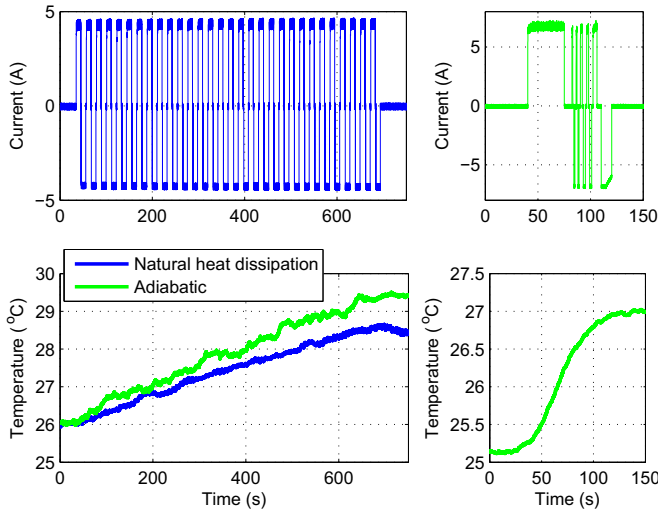


Fig. 7. Temperature measurements for identification of the heat capacitance C_{heat} , heat transfer coefficient h , and geometric parameter a .

4. Extended Kalman filter scheme

The extended Kalman filter (EKF) algorithm constitutes a robust and efficient observer for nonlinear systems, as it is the case for the voltage and temperature dependence of ultracapacitors. Details about the EKF algorithm can be found in Refs. [18,28]. In this section, the EKF technique is applied to the extended model developed in Section 3. Although the EKF approach is standard, its application to ultracapacitor SOC and temperature estimation requires careful selection of extended states and covariance matrices. To simplify computations and to implement the EKF for realtime application, the extended model in Eq. (1), which is detailed in Eq. (9), is first discretized using Euler's approximation [29].

$$\begin{aligned} x_{k+1} &= f_k(x_k, u_k) + w_k \\ z_k &= h_k(x_k, u_k) + v_k \end{aligned} \quad (13)$$

where $x_k = [\text{SOC} \ V_1 \ V_2 \ T]^T_k$ is the extended state vector at instant $k\Delta t$, given sampling period Δt . The input current i and output voltage V_T are considered measurable. The process noise w_k and measurement noise v_k are considered Gaussian, uncorrelated and centered white noise with zero expectation and their covariance matrices are, respectively: $Q = E[w_k w_k^T]$ and $R = E[v_k v_k^T]$. The application of EKF involves linearization about the current state estimate \hat{x}_k : $F_k = \partial f_k(x_k, u_k) / \partial x_k|_{x_k=\hat{x}_k}$ and $H_k = \partial h_k(x_k, u_k) / \partial x_k|_{x_k=\hat{x}_k}$. Given initial values for the state estimate \hat{x}_k and estimate error covariance matrix P_k , the EKF algorithm consists of recursive computation of the predictor Eqs. (i)–(ii) and the corrector Eqs. (iii)–(v) [18,28]:

- (i) project the state ahead: $\hat{x}_{k+1}^- = f_k(\hat{x}_k, u_k)$,
- (ii) project the error covariance ahead: $P_{k+1}^- = F_k P_k F_k^T + Q$,
- (iii) compute the Kalman gain: $K_{k+1} = P_{k+1}^- H_{k+1}^T [H_{k+1} P_{k+1}^- H_{k+1}^T + R]^{-1}$,
- (iv) update estimate with measurement z_k : $\hat{x}_{k+1} = \hat{x}_{k+1}^- + K_{k+1}(z_{k+1} - H_{k+1} \hat{x}_{k+1}^-)$,
- (v) update the error covariance: $P_{k+1} = (I - K_{k+1} H_{k+1}) P_{k+1}^-$.

5. Experimental results

The performance of the EKF estimator is examined via a series of charge/discharge cycle tests performed on the 100 F PowerBurst

ultracapacitor under different operating conditions. Different sets of ultracapacitor are used in the tests so modeling errors are expected. As the EKF technique lacks convergence criteria and systematic gain tuning procedures, the implementation of the EKF is still a procedure which requires a significant amount of testing and tuning. Specifically, the tuning of the entries of the filter covariance matrices relies heavily on trial-and-error to achieve maximum likelihood state estimation [30]. In this experimental study, covariance matrices in diagonal form are chosen for the EKF estimation: $Q = \text{diag}(0.4, 0.2, 0.06, 0.01)$, $R = 0.15$, the initial value of $P = \text{diag}(0.1, 0.1, 0.1, 0.1)$, and the sampling time $\Delta t = 10$ ms. The experiments are conducted considering three different cases corresponding to different operating conditions: (i) charge/discharge test with asymmetrical current rates close to adiabatic condition, (ii) scaled current from a Toyota Prius in NYCC driving cycle under natural heat dissipation condition, and (iii) charge/discharge test at -38°C .

5.1. Charge/discharge test with asymmetrical current rates close to adiabatic condition

Fig. 8 shows the asymmetrical current profile used in this test. The ultracapacitor is charged with 7.2 A and discharged with 3.6 A at a constant frequency (180 mHz). The ultracapacitor along with the platinum thin-film temperature sensor are wrapped with a ceramic fiber blanket for heat insulation so the heat transfer coefficient h in Eq. (6) is considered zero in this case. The ambient temperature in the controlled climatic chamber is 32°C . Fig. 8 shows that during the asymmetrical charge/discharge cycles, the cell temperature T gradually raises from 32.1°C to 35.3°C whereas the terminal voltage V_T and the state of charge (SOC) build up during each charge and decline during each discharge. The terminal voltage varies between 1 V and 2 V while the SOC ranges from 0.39 to 0.65 during this cycle test. The predictions made by the nonlinear model and the EKF estimator are compared with the voltage and temperature measurements. Zoomed-in views of the terminal voltage V_T in Figs. 8 and 9 show that the model prediction error of the terminal voltage V_T gradually builds up as the charge increases owing to the modeling error of the capacitance. On the other hand, the EKF estimator achieves better and more consistent prediction of terminal voltage and more precise prediction of steady state temperature by simultaneously taking into consideration of the modeling uncertainties and measurement noises. Specifically, the EKF estimator achieves maximum voltage estimation error of about 50 mV and maximum temperature estimation error of about 0.35°C . Zoomed-in views of the SOC in Fig. 8 show that the predictions made by the nonlinear model and the EKF estimator stay close initially but diverge at the end of the test cycles as the charge increases. This difference is again induced by the modeling error of the capacitance.

5.2. Scaled current from a Toyota Prius in NYCC driving cycle under natural heat dissipation condition

In this test, the capability of the EKF estimator developed for ultracapacitor SOC and thermal estimation in HEV application is examined following the main test used in Ref. [21]. Two successive NYCC driving cycles are applied to a Toyota Prius in the ADVISOR model [31,32] in which the Ni–MH batteries are replaced with an energy storage system containing 600 modules of 2.1 Ah Maxwell ultracapacitor in series-parallel configuration. For the cycle test with the 100 F PowerBurst ultracapacitor, the charge/discharge current in the 2nd driving cycle is scaled to 1/24 and the initial SOC is set to 0.92. The heat transfer coefficient $h = 7 \text{ W m}^{-2} \text{ K}^{-1}$ under natural heat dissipation condition is identified from the

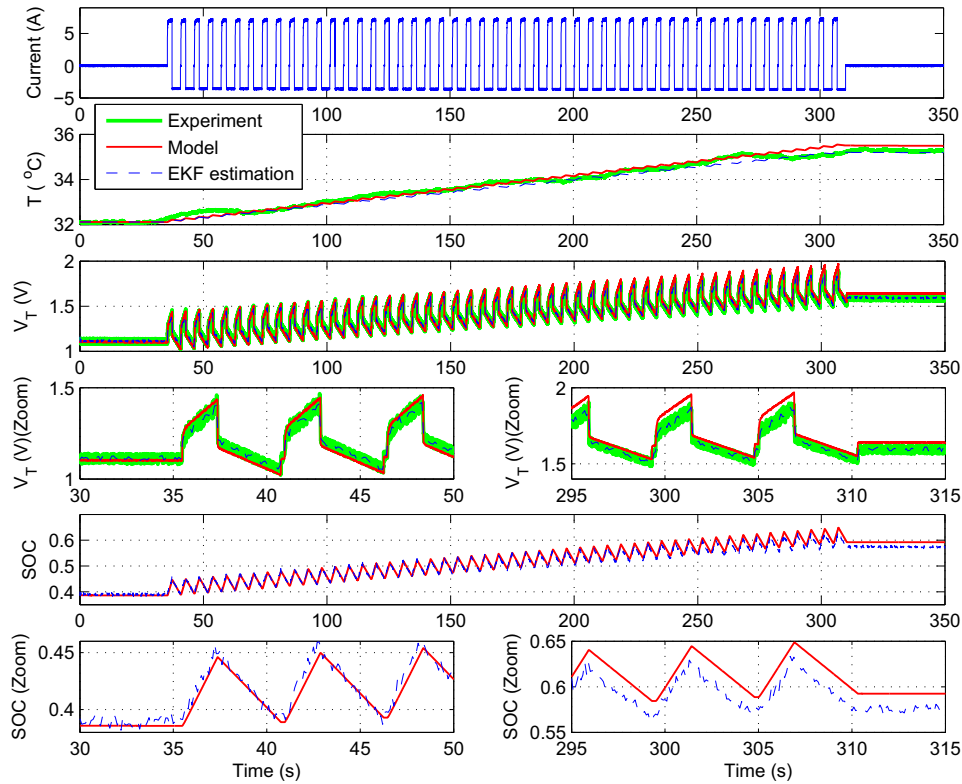


Fig. 8. Case (i): estimation of temperature, terminal voltage and SOC when the ultracapacitor is charged and discharged with asymmetrical current rates close to adiabatic condition.

temperature measurement in Fig. 10 using the method in Section 3.2.2. The ambient temperature in the controlled climatic chamber is 20 °C. As the test in Fig. 10 contains more discharge cycles than charge cycles, the terminal voltage V_T and the SOC are gradually depleted respectively from 2.51 V to 0.87 V and from 0.92 to 0.29. The ultracapacitor is gradually cooled during this test due to the negative entropy changes in Eq. (8) while discharging ($i < 0$). The cell temperature estimates predicted by the nonlinear model and

the EKF estimator are quite close as limited temperature variation is observed in this case. The EKF estimator, however, achieves better and more consistent prediction of the terminal voltage V_T with 40 mV maximum estimation error.

5.3. Charge/discharge test at −38 °C

To evaluate the performance of the EKF estimator at extremely low temperature, this charge/discharge test is conducted at ambient temperature of −38 °C controlled by the climatic chamber. Fig. 11 shows the charge/discharge current profile, the cell temperature T , the terminal voltage V_T and the SOC. The heat transfer coefficient $h = 10.5 \text{ W m}^{-2} \text{ K}^{-1}$ is identified from the temperature measurement in Fig. 11 using the method in Section 3.2.2. With an initial terminal voltage of 2 V, the ultracapacitor is charged and discharged with 6.5 A current at a constant frequency 66 mHz. The model overestimates the terminal voltage V_T and thus SOC during each charge due to the underestimated values of capacitance C . Significant voltage drop at the end of each charging period is observed due to the increased series resistance R_s at low temperature. As the cell temperature raises from −38.1 °C to −24.3 °C during the charge/discharge cycles, significant changes in the resistance R_s and the capacitance C are expected from Fig. 5. As a result, Fig. 11 shows that the peak-to-peak values of the terminal voltage V_T and SOC gradually shrink. Fig. 12 shows the estimation errors of the terminal voltage and the cell temperature. Larger modeling error is observed in this case as the parameters R_s , C and τ are more sensitive to temperature variation at low temperature as illustrated in Fig. 5 and the cell temperature also raises faster due to higher resistance R_s at low temperature and higher charge/discharge currents. The EKF estimator, on the other hand, is able to provide significantly better estimation of the terminal voltage and

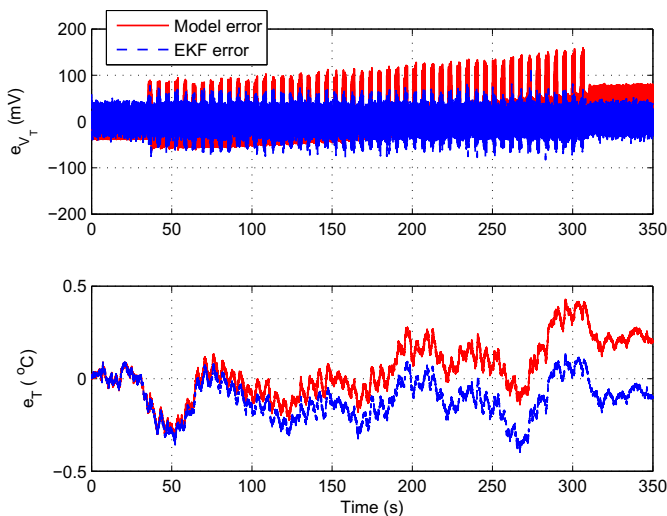


Fig. 9. Case (i): prediction errors of the terminal voltage and temperature when the ultracapacitor is charged and discharged with asymmetrical current rates close to adiabatic condition.

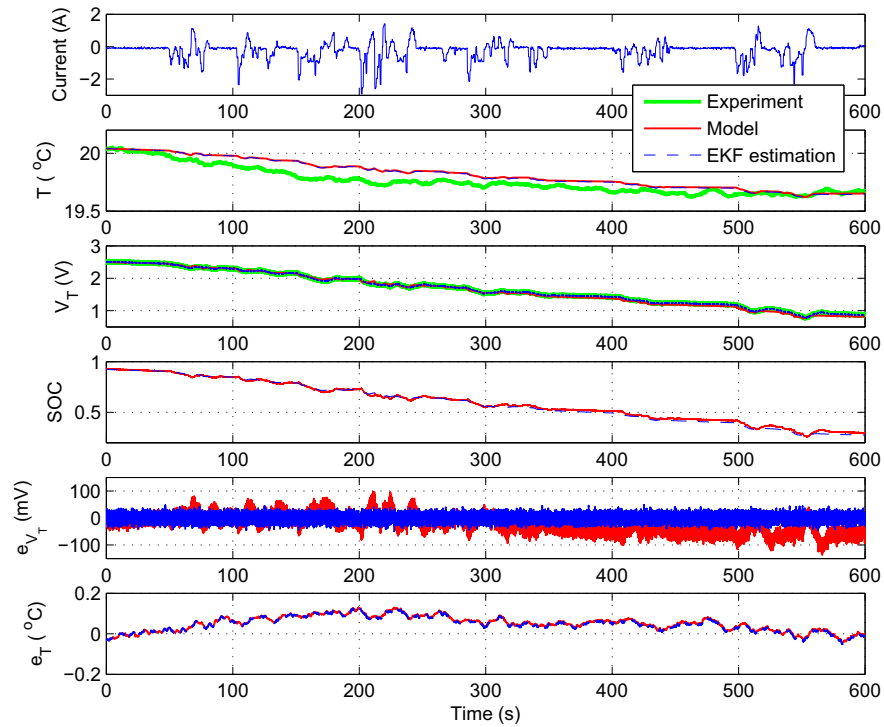


Fig. 10. Case (ii): estimation of temperature, terminal voltage and SOC when the ultracapacitor is charged and discharged with a scaled current profile from a Toyota Prius in NYCC driving cycle under natural heat dissipation condition.

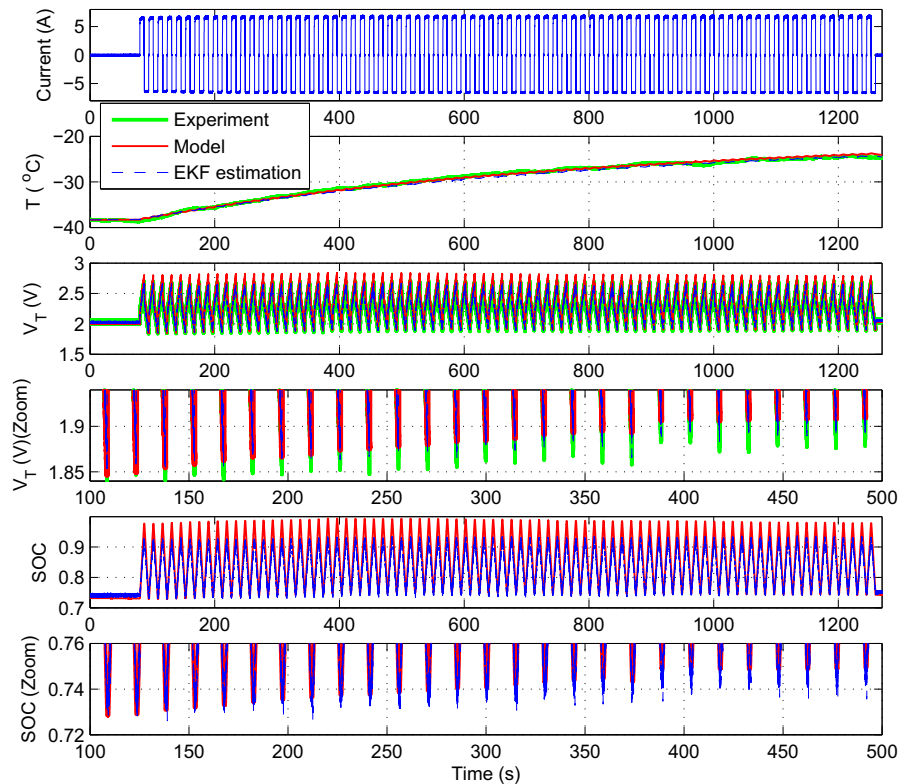


Fig. 11. Case (iii): estimation of temperature, terminal voltage and SOC when the ultracapacitor is charged and discharged at -38°C .

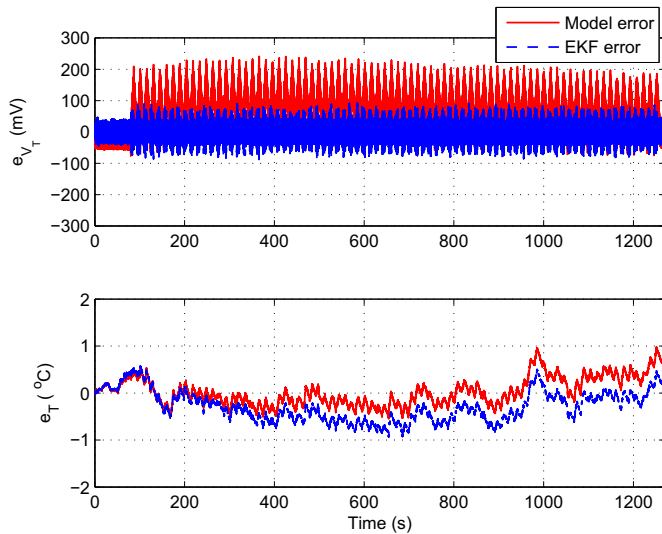


Fig. 12. Case (iii): prediction errors of the terminal voltage and temperature when the ultracapacitor is charged and discharged at $-38\text{ }^{\circ}\text{C}$.

thus the SOC. Specifically, the EKF estimator achieves maximum voltage estimation error of about 80 mV and maximum temperature estimation error of about $0.9\text{ }^{\circ}\text{C}$.

6. Conclusions

For optimum energy and thermal management of the ultracapacitor, a novel EKF-based estimator is proposed in this paper to achieve simultaneous estimation of the state-of-charge (SOC) and cell temperature in existence of modeling uncertainties and measurement noises. For the application of EKF algorithm, a non-linear ultracapacitor model which consists of a voltage-and-thermal-dependent equivalent circuit model and a thermal model is first developed. The parameters in the equivalent circuit model are identified by applying least squares method with weightings at different frequencies so as to achieve satisfactory prediction over the whole applicable frequency ranges. On the other hand, the parameters in the thermal model are identified based on the temperature measurement of the ultracapacitor when it is charged and discharged with different current profiles under different heat transfer conditions. To examine the robustness of the EKF-based estimator to modeling errors, different sets of ultracapacitor are used in three tests corresponding to different operating conditions. Experimental results show that the EKF-based estimator achieves improved and consistent prediction of the state-of-charge and temperature in different scenarios. The advantage of the EKF-based estimator over the open-loop prediction is more significant during dynamic charge/discharge cycles at extremely low temperature as the impact of modeling uncertainties becomes more noteworthy. The model-based EKF algorithm also allows estimation of other states and parameters if they are included in the extended model. For instance, by augmenting the aging model in Ref. [9] to the extended model, the degradation or lifetime of the ultracapacitor can be estimated. Another extension of this work is to estimate the thermal dynamics and SOC of ultracapacitors using other variants of Kalman filter, which have been successfully applied to battery SOC estimations [22–25,33–36].

Acknowledgments

This work was supported by the National Science Council, Taiwan, ROC, under Grant NSC-100-2628-E011-016-MY2.

Appendix. Variables and parameters

Table 2

List of all parameters and their values, if constant.

	Definition	Value
τ	Time constant, s	
Δt	Sampling time, ms	10
a	Geometric factor	2
a_{ω_i}	Weighting at frequency ω_i	
A	Effective heat transfer area, m^2	0.0044
c_1	Coefficient of polynomial approximation	1.847319×10^9
c_2	Coefficient of polynomial approximation	-2.1075175×10^8
c_3	Coefficient of polynomial approximation	-6.5652681×10^8
c_4	Coefficient of polynomial approximation	1.286392774×10^6
c_5	Coefficient of polynomial approximation	-1.683916084×10^6
c_6	Coefficient of polynomial approximation	-7.905128205×10^6
c_7	Coefficient of polynomial approximation	$-2.78391608392 \times 10^4$
c_8	Coefficient of polynomial approximation	$1.5673167832168 \times 10^2$
c_9	Coefficient of polynomial approximation	$-7.598443463245 \times 10^3$
c_{10}	Coefficient of polynomial approximation	$3.0393964635297 \times 10^2$
c_{11}	Coefficient of polynomial approximation	-0.435124370975963
c_{12}	Coefficient of polynomial approximation	2.104245538015005
c_{13}	Coefficient of polynomial approximation	-0.454357816299
c_{14}	Coefficient of polynomial approximation	2.3693043249053
c_{15}	Coefficient of polynomial approximation	26.0539561941699
c_{16}	Coefficient of polynomial approximation	152.0162483594322
c_{17}	Coefficient of polynomial approximation	4.5465034×10^8
c_{18}	Coefficient of polynomial approximation	6.1330481×10^7
c_{19}	Coefficient of polynomial approximation	-8.600148199×10^6
c_{20}	Coefficient of polynomial approximation	$-3.1971222487 \times 10^5$
c_{21}	Coefficient of polynomial approximation	$-8.56795966943 \times 10^4$
c_{22}	Coefficient of polynomial approximation	$1.3920291658325 \times 10^2$
C	Equivalent series capacitance, F	
C_{heat}	Heat capacitance, J K^{-1}	37
e	Elementary charge, C	1.602×10^{-19}
h	Heat transfer coefficient, $\text{Wm}^{-2} \text{K}^{-1}$	0 (Adiabatic) 7–13 (Natural heat dissipation)
$Im_{\omega_i, \text{data}}$	Imaginary part of the EIS measurement at frequency ω_i , m Ω	
k_b	Boltzmann constant, J K^{-1}	$1.3806515 \times 10^{-23}$
Q_{joule}	Irreversible Joule heat, J	
Q_{rev}	Reversible Joule heat, J	
$Re_{\omega_i, \text{data}}$	Real part of the EIS measurement at frequency ω_i , m Ω	
R_s	Equivalent series resistance, m Ω	
SOC	State of charge	
V_1	Voltage of the 1st parallel RC circuit, mV	
V_2	Voltage of the 2nd parallel RC circuit, mV	
V_s	Voltage of the equivalent series resistance, V	
V_T	Terminal voltage of the ultracapacitor, V	

References

- [1] J. Schiffer, D. Linzen, D.U. Sauer, J. Power Sources 160 (2006) 765–772.
- [2] D.H. Lee, U.S. Kim, C.B. Shin, B.H. Lee, B.W. Kim, Y.H. Kim, J. Power Sources 175 (2008) 664–668.
- [3] A. Burke, J. Power Sources 91 (2000) 37–50.
- [4] A.G. Pandolfo, A.F. Hollenkamp, J. Power Sources 157 (2006) 11–27.
- [5] W.G. Pell, B.E. Conway, J. Power Sources 136 (2004) 334–345.
- [6] B. Frenzel, P. Kurzweil, H. Rönnebeck, J. Power Sources 196 (2011) 5364–5376.
- [7] D. Rotenberg, A. Vahidi, I. Kolmanovsky, IEEE Trans. Control Syst. Technol. 19 (2011) 576–589.
- [8] D. Iannuzzi, P. Tricoli, IEEE Trans. Power Electron. 27 (2012) 2129–2140.
- [9] O. Bohlen, J. Kowal, D.U. Sauer, J. Power Sources 173 (2007) 626–632.
- [10] R. Kötz, M. Hahn, R. Gallay, J. Power Sources 154 (2006) 550–555.
- [11] H. Michel, J. Power Sources 154 (2006) 556–560.
- [12] S.I. Fletcher, F.B. Sillars, R.C. Carter, A.J. Cruden, M. Mirzaei, N.E. Hudson, J.A. Parkinson, P.J. Hall, J. Power Sources 195 (2010) 7484–7488.
- [13] M.A. Sakka, H. Gualous, J.V. Mierlo, H. Culcu, J. Power Sources 194 (2009) 581–587.

- [14] S. Buller, E. Karden, D. Kok, R.W. De Doncker, IEEE Trans. Ind. Appl. 38 (2002) 1622–1626.
- [15] H. Gualous, D. Bouquain, A. Berthon, J.M. Kauffmann, J. Power Sources 123 (2003) 86–93.
- [16] F. Rafik, H. Gualous, R. Gallay, A. Crausaz, A. Berthon, J. Power Sources 165 (2007) 928–934.
- [17] C.H. Wu, Y.H. Hung, C.W. Hong, Energy Convers. Manag. 53 (2012) 337–345.
- [18] G.L. Plett, J. Power Sources 134 (2004) 252–261.
- [19] G.L. Plett, J. Power Sources 134 (2004) 262–276.
- [20] G.L. Plett, J. Power Sources 134 (2004) 277–292.
- [21] A. Vasebi, M. Partovibakhsh, S.M.T. Bathaee, J. Power Sources 174 (2007) 30–40.
- [22] G.L. Plett, J. Power Sources 161 (2006) 1356–1368.
- [23] G.L. Plett, J. Power Sources 161 (2006) 1369–1384.
- [24] S. Santhanagopalan, R.E. White, Int. J. Energy Res. 34 (2010) 152–163.
- [25] J. Zhang, C. Xia, Electrical Power Energy Syst. 33 (2011) 472–476.
- [26] X. Hu, S. Li, H. Peng, F. Sun, J. Power Sources 217 (2012) 209–219.
- [27] Maxwell BC, Series Ultracapacitor Datasheet (January 2013). www.maxwell.com/products/ultracapacitors/docs/datasheet_bc_series_1017105.pdf.
- [28] E. Wan, A. Nelson, Dual extended Kalman filter methods, in: S. Haykin (Ed.), Kalman Filtering and Neural Networks, Wiley/Interscience, New York, 2001, pp. 123–174.
- [29] K. Ogata, Discrete-time Control Systems, Prentice-Hall International, 1987.
- [30] G. Welch, G. Bishop, An Introduction to the Kalman Filter, UNC, Chaple Hill, 2002.
- [31] T. Markel, A. Brooker, T. Hendricks, V. Johnson, K. Kelly, B. Kramer, M. O'Keefe, S. Sprik, K. Wipke, J. Power Sources 110 (2002) 255–266.
- [32] V.H. Johnson, J. Power Sources 110 (2002) 321–329.
- [33] J.Y. Han, D.C. Kim, M. Sunwoo, J. Power Sources 188 (2009) 606–612.
- [34] J. Wang, J. Guo, L. Ding, Energy Convers. Manag. 50 (2009) 3182–3186.
- [35] F. Sun, X. Hu, Y. Zou, S. Li, Energy 36 (2011) 3531–3540.
- [36] D. Andre, C. Appel, T. Soczka-Guth, D.U. Sauer, J. Power Sources 224 (2013) 20–27.